Draft version August 16, 2022
Typeset using LaTeX twocolumn style in AASTeX631

The location of features in the mass distribution of merging binary black holes does not depend on the metallicity-dependent cosmic star formation.

L. A. C. van Son[1, 2, 3] and et. al

[1] Center for Astrophysics | Harvard & Smithsonian, 60 Garden St., Cambridge, MA 02138, USA
[2] Anton Pannekoek Institute of Astronomy and GRAPPA, Science Park 904, University of Amsterdam, 1098XH Amsterdam, The Netherlands
[3] Max Planck Institute for Astrophysics, Karl-Schwarzschild-Str. 1, 85748 Garching, Germany

ABSTRACT

New observational facilities are probing astrophysical transients such as stellar explosions and gravitational wave (GW) sources at ever increasing redshifts. To interpret these observation we need to compare them to predictions from stellar population models. These models, require the metallicity-dependent star formation rate density ($\mathcal{S}(Z, z)$) as an input. Large uncertainties remain in the shape and evolution of this function, and understanding its behaviour is essential to explain simulation results. In this work, we propose a simple analytical function for $\mathcal{S}(Z, z)$. Variations of this function can be easily interpreted, because the parameters link to its shape in an intuitive way. We fit our analytical function to the star-forming gas of the cosmological TNG100 simulations and find that it is able to capture the main behaviour well. As an example application, we investigate the effect of systematic variations in the $\mathcal{S}(Z, z)$ parameters on the predicted mass distribution of locally merging binary black holes (BBH). Our main findings are I) the location of features is remarkably robust against variations in the metallicity-dependent star formation rate and II) the low mass end is least affected by these variations. This is promising as it increases our chances to constrain the physics that governs the formation of these objects. We further find that III) the skewness, mean, and width of the metallicity distribution at low redshift affect the overall rate, while IV) the redshift evolution of the width and the mean of the metallicity distribution affects the slope at the high-mass end of the distribution.

1. INTRODUCTION

A myriad of astrophysical phenomena depend critically on the rate of star formation throughout the cosmic history of the Universe. Exotic transient phenomena, including (pulsational) pair-instability supernovae, long gamma-ray bursts and gravitational wave (GW) events appear to be especially sensitive to the metallicity at which star formation occurs at different epochs throughout the Universe (e.g., Langer et al. 2007; Fruchter et al. 2006; Abbott et al. 2016). Gravitational astronomy in particular has seen explosive growth in the number of detections in the past decade (Abbott et al. 2018, 2020, 2021a). In order to correctly model and interpret these observations, it is fundamental to know the rate of star formation at different metallicities throughout cosmic history, i.e. the metallicity-dependent star formation rate density ($\mathcal{S}(Z, z)$, see also the recent review by Chruślińska 2022). Throughout this work little z refers to the redshift and Z the metallicity of star formation.

Corresponding author: L. van Son
lieke.van.son@cfa.harvard.edu

It is difficult to observationally constrain the shape of $\mathcal{S}(Z, z)$, see Chruślińska & Nelemans (2019) for an extensive overview and discussion of relevant observational caveats. Even at low redshifts, the low metallicity part of the distribution is poorly constrained (Chruślińska et al. 2021). Nonetheless, several methods exist to estimate the metallicity dependent star-formation rate.

The first method combines a galaxy mass-metallicity relation, MZ-relation and a galaxy stellar mass function, GSMF (see e.g. Dominik et al. 2013). However, the applied methods to infer galaxy properties and subsequently scaling relations such as the MZ-relation differ greatly, which makes it difficult to interpret these results in a consistent way (e.g., Kewley & Ellison 2008; Maiolino & Mannucci 2019; Cresci et al. 2019). Moreover, observations are generally incomplete at high redshifts and low galaxy luminosity (e.g., Chruślińska et al. 2021).

One can also directly extract the metallicity density fraction from cosmological simulations (e.g. Mapelli et al. 2017; Briel et al. 2021). However, these simulations currently lack the resolution to resolve the lowest mass galaxies, and their variations in $\mathcal{S}(Z,z)$ span a smaller range than those observed in observationally-based models (Pakmor et al. 2022).

Alternatively, one can combine analytical models for the observed star formation rate, $\mathrm{SFRD}(z)$, like those from Madau & Dickinson (2014) or Madau & Fragos (2017), and convolve this with an assumed function for the shape of the shape of the metallicity density distribution, such as was was done in e.g., Langer & Norman (2006a); Neijssel et al. (2019).

In this work we follow the latter approach and propose a flexible analytical model for the $\mathcal{S}(Z,z)$ that can be fit to the output of both cosmological simulations, and observational data constraints where available. In contrast to earlier work, we adopt a skewed-lognormal distribution of metallicities that can capture the asymmetry in the low and high metallicity tails.

The purpose of this proposed form is twofold. First of all, the form we propose allows for an intuitive interpretation of the free parameters. This allows us to get better insight of the impact of changes in these parameters on the inferred ranges of astrophysical transients (as we demonstrate in Section 4 using GW predictions as an example). By adopting an analytical, parametrized form for $\mathcal{S}(Z,z)$, the large uncertainties can be systematically explored. Secondly, both the large complications in observational constraints, and the many uncertainties in cosmological simulations call for a generalised form of the $\mathcal{S}(Z,z)$ that can be easily updated when new information becomes available. In particular, the advent of observations with the James Webb Space Telescope promises a new era of high-redshift metallicity studies of previously unexplored regimes (e.g., Sanders et al. 2022). We hope that this form will facilitate the flexibility needed to keep up with observations.

We describe our model for $\mathcal{S}(Z,z)$ in Section 2. We fit our model to to the star-forming gas in the Illustris TNG100 simulation in Section 3 we demonstrate an example application of our model by systematically varying the parameters that determine the shape of $\mathcal{S}(Z,z)$ and investigate their impact on the local distribution of merging BBH masses in Section 4. We summarise our findings in Section 5.

Throughout this work, we adopt a Kroupa initial mass function (Kroupa 2001) and a flat ΛCDM cosmology with $\Omega_\mathrm{M} = 0.31$, $\Omega_\Lambda = 0.69$ and $H_0 = 67.7\mathrm{km\,s^{-1}\,Mpc^{-1}}$ (Planck Collaboration et al. 2020).

2. A CONVENIENT ANALYTIC EXPRESSION FOR THE METALLICITY-DEPENDENT STAR FORMATION RATE DENSITY

We assume that the metallicity dependent star formation rate density can be separated into two independent functions (e.g. Langer & Norman 2006b),

$$\boxed{\mathcal{S}(Z,z) = \mathrm{SFRD}(z) \times \frac{\mathrm{dP}}{\mathrm{dZ}}(Z,z).} \tag{1}$$

The first term is the star formation rate density, $\mathrm{SFRD}(z)$, that is the amount of mass formed in stars per unit time and per unit comoving volume at each redshift, z. The second term, $\mathrm{dP/dZ}(Z,z)$, is a probability density function that expresses what fraction of star formation occurs at which metallicity, Z, at each redshift.

2.1. *The metallicity probability density function*

For the probability distribution of metallicities we draw inspiration from the approach by e.g., Neijssel et al. (2019) who used a log-normal distribution. Unfortunately, this expression does not capture the asymmetry well that we see in the results of the cosmological simulations, which show an extended tail in $\log_{10} Z$ towards low metallicity, combined with a very limited tail towards higher metallicity. To capture this behaviour we adopt a skewed-log-normal distribution instead. This is an extension of the normal distribution that introduces an additional shape parameter, α, that regulates the skewness (first introduced by O'Hagan & Leonard 1976).

The skewed-log-normal distribution of metallicities is defined as:

$$\begin{aligned}\frac{\mathrm{dP}}{\mathrm{dZ}}(Z) &= \frac{1}{Z} \times \frac{\mathrm{dP}}{\mathrm{d}\ln Z} \\ &= \frac{1}{Z} \times \frac{2}{\omega} \underbrace{\phi\left(\frac{\ln Z - \xi}{\omega}\right)}_{(a)} \underbrace{\Phi\left(\alpha\frac{\ln Z - \xi}{\omega}\right)}_{(b)},\end{aligned} \tag{2}$$

where (a) is the standard log-normal distribution, ϕ,

$$\phi\left(\frac{\ln Z - \xi}{\omega}\right) \equiv \frac{1}{\sqrt{2\pi}} \exp\left\{-\frac{1}{2}\left(\frac{\ln Z - \xi}{\omega}\right)^2\right\} \tag{3}$$

and (b) is the new term that allows for asymmetry, which is equal to the cumulative of the log-normal distribution, Φ,

$$\Phi\left(\alpha\frac{\ln Z - \xi}{\omega}\right) \equiv \frac{1}{2}\left[1 + \mathrm{erf}\left\{\alpha\frac{\ln Z - \xi}{\omega\sqrt{2}}\right\}\right] \tag{4}$$

This introduces three parameters, α, ω and ξ, each of which may depend on redshift. The first parameter, α, is known as the "shape". It affects the skewness of the distribution and thus allows for asymmetries between metallicities that are higher and lower than the mean. The symmetric log-normal distribution is recovered for $\alpha = 0$. The second parameter, ω is known as the "scale". It provides a measure of the spread in metallicities at each redshift. Finally, ξ, is known as the "location", because this parameter plays a role in setting the mean of the distribution at each redshift.

The location and the mean of the metallicity distribution— To obtain a useful expression for the redshift dependence of the "location" $\xi(z)$ we first express the expectation value or mean metallicity at a given redshift

$$\langle Z \rangle = 2\exp\left(\xi + \frac{\omega^2}{2}\right)\Phi\left(\beta\,\omega\right) \tag{5}$$

where β is

$$\beta = \frac{\alpha}{\sqrt{1+\alpha^2}}. \tag{6}$$

For a more extended derivation of the moments of the skewed-log-normal, see e.g., Wang et al. (2019).
For the evolution of the mean metallicity with redshift we follow Langer & Norman (2006b) and Neijssel et al. (2019) in assuming that the mean of the probability density function of metallicities evolves with redshift as:

$$\langle Z \rangle \equiv \mu(z) = \mu_0 \cdot 10^{\mu_z \cdot z}, \tag{7}$$

where μ_0 is the mean metallicity at redshift 0, and μ_z determines redshift evolution of the location. Equating this to Equation 5, we get an expression for $\xi(z)$,

$$\xi(z) = \ln\left(\frac{\mu_0 \cdot 10^{\mu_z \cdot z}}{2\,\Phi(\beta\,\omega)}\right) - \frac{\omega^2}{2}. \tag{8}$$

The scale (and variance) of the metallicity distribution— We will also allow the "scale" ω to evolve with redshift in a similar manner,

$$\omega(z) = \omega_0 \cdot 10^{\omega_z \cdot z}. \tag{9}$$

where ω_0 is the width of the metallicity distribution at $z = 0$, and ω_z the redshift evolution of the scale.

Note that the width, $w(z)$ is not the same as the variance. The variance, $\sigma(z)^2$, can be expressed as

$$\sigma(z)^2 = \omega(z)^2\left(1 - \frac{2\beta^2}{\pi}\right) \tag{10}$$

Asymmetry of the metallicity distribution: α—The skewness α could in principle also be allowed to evolve with redshift (e.g., $\alpha(z) = \alpha(z=0)10^{\alpha_z \cdot z}$). However, we find no significant improvement over the simpler assumption where alpha is kept constant. Note that the redshift evolution of the 'scale' (eq. 9), already captures similar behaviour in our current formalism. We therefore adopt $\alpha = \alpha(z=0)$ and $\alpha_z = 0$.

In summary, Equation 2 becomes:

$$\boxed{\frac{\mathrm{dP}}{\mathrm{dZ}}(Z,z) = \frac{2}{\omega(z)Z} \times \phi\left(\frac{\ln Z - \xi(z)}{\omega(z)}\right)\Phi\left(\alpha\frac{\ln Z - \xi(z)}{\omega(z)}\right)}, \tag{11}$$

where $\xi(z)$ and $\omega(z)$ are defined in Equations 8 and 9 respectively and we have assumed α to be constant.

2.2. *The overall cosmic star formation rate density*

For the star formation rate density, we assume the analytical form proposed by Madau & Dickinson (2014),

$$\boxed{\mathrm{SFRD}(z) = \frac{d^2 M_{\rm SFR}}{dt dV_c}(z) = a\frac{(1+z)^b}{1+\left[(1+z)/c\right]^d}} \tag{12}$$

in units of $\left[\mathrm{M}_\odot\,\mathrm{yr}^{-1}\,\mathrm{cMpc}^{-3}\right]$. This introduces four parameters; a which sets the overal normalisation and which has the same units as SFRD(z) and b, c and d which are unitless and which govern the shape of the overal cosmic star formation rate density with redshift.

Lastly, we combine equations 11 and 12 to form a full metallicity specific star formation rate density as described in equation 1.

3. FIT AGAINST COSMOLOGICAL SIMULATION

We fit our new functional form of $\mathcal{S}(Z,z)$ as defined by equations 1, 11 and 12 to the Illustris-TNG cosmological simulations. We simultaneously fit for the following nine free parameters $\alpha, \mu_0, \mu_z, \omega_0, \omega_z$, which govern the metallicity dependence and a, b, c and d, which set the overall star formation rate.

Below we briefly discuss the Illustris-TNG simulations, and elaborate on our fitting procedure.

3.1. *Illustris-TNG Cosmological simulations*

Although here, we only fit our model to the TNG100 simulation, our prescription can be easily be used to fit other simulated or observational data of the metallicity dependent star formation rate density[1].

The IllustrisTNG-project (or TNG in short, Springel et al. 2018; Marinacci et al. 2018; Nelson et al. 2018; Pillepich et al. 2018a; Naiman et al. 2018) considers galaxy formation and evolution through large-scale cosmological hydrodynamical simulations. Such simulations provide the tools to study parts of the Universe

[1] We provide a Jupyter notebook to facilitate this fit here: https://github.com/LiekeVanSon/SFRD_fit/blob/main/src/scripts/Fit_To_Cosmological_Simulation.ipynb

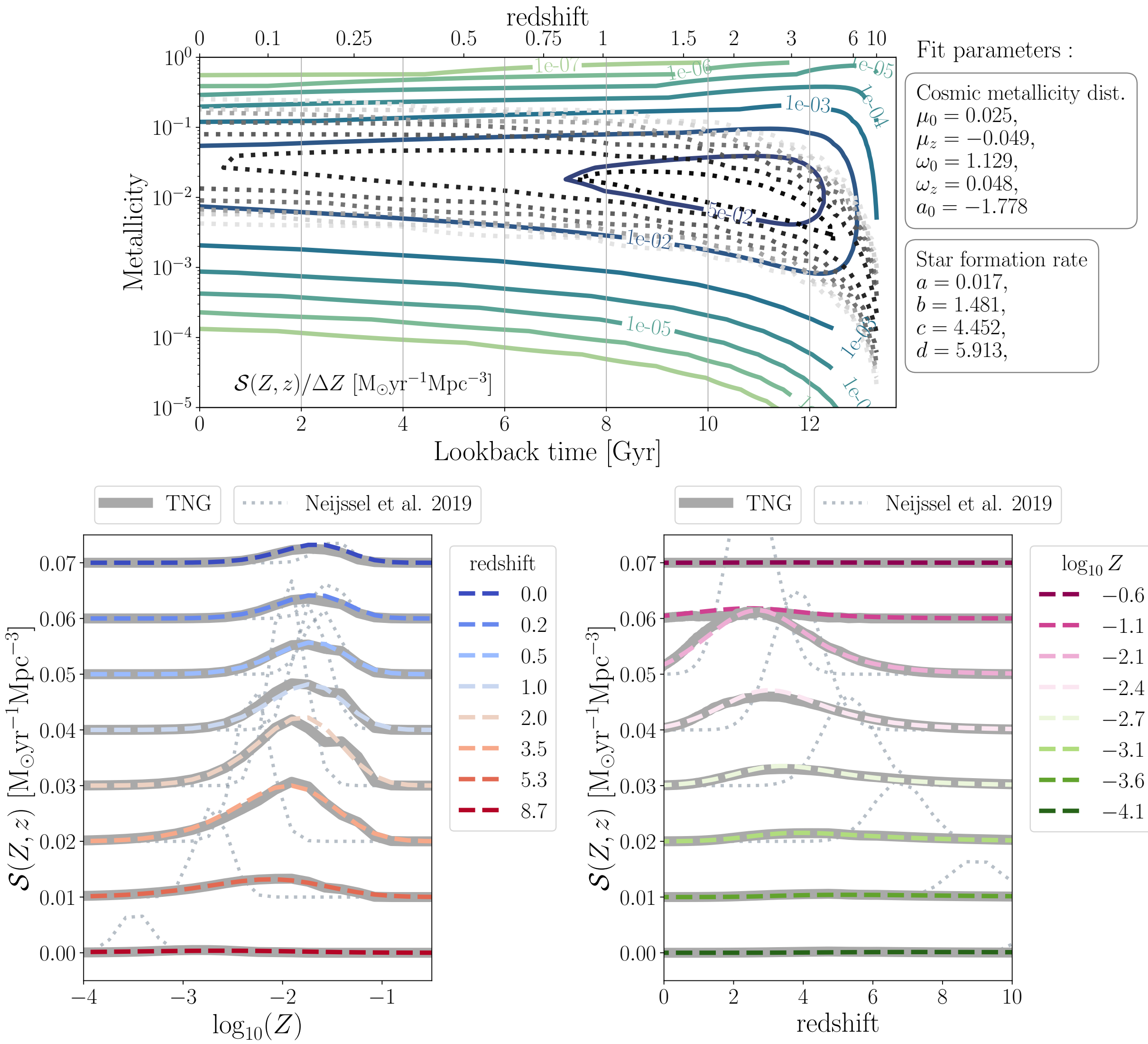

Figure 1. Our fiducial $\mathcal{S}(Z,z)$ model, adopting the best fitting parameters (listed on the top right) to fit the TNG100 simulations. The top panel shows the full two dimensional $\mathcal{S}(Z,z)$ linear in time. The bottom left (right) panel shows slices of the distribution in redshift (metallicity). Each slice is displaced by $0.01\mathrm{M_\odot\,yr^{-1}\,Mpc^{-3}}$. We show the TNG100 simulation data with thick gray lines. For comparison, we also show the phenomenological model from Neijssel et al. (2019) in each panel with grey dotted lines. For the latter, the contours in the top panel range from $10^{-7} - 10^{-2}\mathrm{M_\odot\,yr^{-1}\,Mpc^{-3}}$. This shows that our analytical model adequately captures the $\mathcal{S}(Z,z)$ of the TNG100 simulations.

that are not easily accessible by observations. In particular of interest for this work, they simulate the high redshift enrichment of galaxies and the tail of low metallicity star formation at low redshift.

The models implemented in the publicly available TNG simulations[2] have lead to many successes. For a more extended discussion focused on the processes that govern the creation, distribution and mixing of metals in in the TNG simulations we refer to Pakmor et al. (2022). In short, star formation in the TNG simulations is calibrated against the Kennicutt–Schmidt relation (Schmidt 1959; Kennicutt 1989). The stellar metallicity yields are an updated version of the original Illustris simulations as described in Pillepich et al. (2018b). Star particles deposit metals into the gas through type Ia and type II supernovae, as well as through asymptotic giant branch stars. The TNG simulations have been shown to match observational constraints on the mass-metallicity relation of galaxies up to $z = 2$ (Torrey et al. 2019), as well as iron abundances (Naiman et al. 2018) and the metallicity gradients within galaxies at low redshift (Hemler et al. 2021). Several studies have used the TNG simulations to make predictions

[2] https://www.tng-project.org/

for astronomical transient sources (e.g. Briel et al. 2021; Bavera et al. 2022; van Son et al. 2022). In particular, Briel et al. (2021) show that the $\mathcal{S}(Z, z)$ from the TNG and the EAGLE (Schaye et al. 2015; Crain et al. 2015) simulations provide the best agreement between observed and predicted cosmic rates for electromagnetic and gravitational-wave transients.

On the other hand, large uncertainties and crude approximations remain in all contemporary cosmological simulations, thus also in the TNG simulations. For example, dust is not included in the TNG simulations, which could mean that metallicity of the star-forming gas is overestimated. Furthermore, all stellar winds mass loss from massive stars, binary interactions and their ionising effects are ignored (e.g. Dray et al. 2003; Smith 2014; Götberg et al. 2020; Doughty & Finlator 2021; Farmer et al. 2021; Goswami et al. 2022). Moreover, the uniform ionising UV background is turned on abruptly at $z = 6$, which crucially impacts the amount of low metallicity star formation at low redshift.

3.2. *Choices and binning of the data*

We fit equation 1 to the metallicity-dependent star formation rate of the star-forming gas in the TNG100 simulation. For this we use a binned version of the TNG data $\mathcal{S}(Z, z)_{\rm sim}$. We consider metallicities between $\log_{10} Z = -5$ to $\log_{10} Z = 0$ in 30 bins, where we use Z_i to refer to the logarithmic centres of the bins. We ignore star formation in metallicities $\log_{10} Z \leq -5$ as this accounts for less than 1% of the total cosmic star formation rate in these simulations. We consider bins in redshifts between $z = 0$ and $z = 10$, with a step size of $dz = 0.05$, where z_j refers to the centres of the bins.

3.3. *Optimisation function*

To find a solution we use a method based on the sum of the quadratic differences between the simulations and our fit function. Using a vanilla χ-squared approach does not serve our purposes very well as it does a poor job in fitting regions where the star formation is very low. Using a χ-squared approach on the logarithm of the function instead places far too much weight on trying to fit the star formation rate in regions where the rate is very low or not even significant. After experimenting, we find that the following approach gives us satisfactory results.

We first consider a given redshift z_j. For this redshift we compute the sum of the squared residuals between the cosmological simulation and our fit.

$$\chi^2(z_j) \equiv \sum_{Z_i} \left(\mathcal{S}(Z_i, z_j)_{\rm sim} - \mathcal{S}(Z_i, z_j)_{\rm fit}\right)^2 \qquad (13)$$

Here, the variable Z_i runs over all redshift bins. We are particularly interested in properly fitting the low metallicity star formation at high redshifts. At high redshifts, the overall cosmic star formation rate is generally lower. To ensure that our fit procedure gives sufficient weight to the behaviour at all redshifts, we introduce a penalisation factor to somewhat reduce the contribution of redshifts where the peak of cosmic star formation occurs, while increasing the weight where at redshifts where the overall cosmic star formation rate is lower. To achieve this we divide $\chi^2(z_j)$ by the star formation $\sum_{Z_i} \mathcal{S}(Z_i, z_j)$ per redshift bin before adding the contribution of all redshifts. Our final expression for the cost function reads

$$\chi = \sum_{z_j} \frac{\chi^2(z_j)}{\sum_{Z_i} \mathcal{S}(Z_i, z_j)} \qquad (14)$$

To minimize this cost funciton, we use `scipy.optimize.minimize` from SciPy v1.6.3 which implements the quasi-Newton method of Broyden, Fletcher, Goldfarb, and Shanno (BFGS, Nocedal & Wright 2006).

3.4. *Resulting $\mathcal{S}(Z, z)$*

Our best fitting parameters are listed in Table 1. With these fit parameters, $\chi^2(z_j)$ is smaller than $2 \cdot 10^{-4}$ at any given redshift. We will refer to the $\mathcal{S}(Z, z)$ with the parameters listed in Table 1 as our fiducial model.

In Figure 1 we show our fiducial model at different redshifts and metallicities. We also show the overall rate of star formation SFRD(z) in Figure 2. In general, our analytical model captures the metallicity dependent star formation in the TNG100 simulations well (bottom panels of Figure 1). The skewed-log normal metallicity distribution is able to reproduce the overall behaviour that is observed in TNG100 (bottom left panel, but cf. Pakmor et al. 2022, for an in-depth discussion of low metallicity star formation in the TNG50 simulation). Only minor features like the additional bump just above $\log_{10}(Z) = -2$ at redshift 2 are missed. However, for our purposes, it is more important to prioritise fitting the large scale trends, while we are not so interested in smaller scale fluctuations.

Adopting a skewed-lognormal metallicity distribution allows for a tail of low metallicity star formation out to low redshifts. To emphasise the difference between a skewed-lognormal and a symmetric lognormal distribution, we show the phenomenological model from Neijssel et al. (2019) in dotted grey. Their model falls within the family of functions that is encompassed by our model

Table 1. Best fitting parameters for our $\mathcal{S}(Z, z)$ fit to TNG100 data.

dP/dZ	description	best fit	SFRD(z)	best fit
μ_0	mean metallicity at $z = 0$	0.025 ± 0.001	a	$0.02 \pm 0.05\,\mathrm{M_\odot\,yr^{-1}\,Mpc^{-3}}$
μ_z	z-dependence of the mean	-0.048 ± 0.001	b	1.48 ± 0.01
α	shape (skewness)	-1.767 ± 0.05	c	4.45 ± 0.01
ω_0	scale at $z = 0$	1.125 ± 0.005	d	5.90 ± 0.02
ω_z	z-dependence of the scale	0.048 ± 0.0001		

described in Section 2, but we note that their model is very distinctly different.[3]

4. APPLICATION: SYSTEMATIC VARIATIONS OF $\mathcal{S}(Z, z)$ AND THE EFFECT ON THE MASS DISTRIBUTION OF MERGING BBHS

We will now demonstrate the application of our analytical model by systematically varying the parameters in our fiducial $\mathcal{S}(Z, z)$ model, and investigate their effect on the local mass distribution of BBH mergers originating from isolated binaries.

We use the publicly available rapid binary population synthesis simulations presented in van Son et al. (2022). These simulations were run using version v02.19.04 of the open source `COMPAS` suite (Riley et al. 2022)[4]. `COMPAS` is based on algorithms that model the evolution of massive binary stars following Hurley et al. (2000, 2002) using detailed evolutionary models by Pols et al. (1998). We refer the reader to the methods section of van Son et al. (2022) for a detailed description of our adopted physics parameters and assumptions. Metallicities of each binary system were sampled from a smooth probability distribution to avoid artificial peaks in the BH mass distribution (e.g. Dominik et al. 2015; Kummer 2020). These simulations provide us with an estimate of the yield of BBH mergers per unit of star-forming mass and metallicity.

We combine the aforementioned yield with variations of the fiducial $\mathcal{S}(Z, z)$ model described in this work. By integrating over cosmic history, we obtain the local merger rates of BBH systems, which allow us to construct the distribution of source properties at every redshift. The details of this framework are described in van Son et al. (2022), but also in Broekgaarden et al. (2021a) and Neijssel et al. (2019).

4.1. *Determining reasonable variations of $\mathcal{S}(Z, z)$*

We consider variations in both the shape of the cosmic metallicity distribution $\mathrm{dP/dZ}(Z, z)$, and the shape of the overall star-formation history, $\mathrm{SFRD}(z)$. To determine the range that is reasonably allowed by observations, we compare our variations to the observation-based $\mathcal{S}(Z, z)$ models described in Chruślińska et al. (2021).

For the cosmic metallicity distribution, we vary every parameter that determines the shape of $\mathrm{dP/dZ}(Z, z)$ independently (left two columns of Table 1). For every variation, we inspect the fraction of stellar mass that is formed at low-metallicity ($Z < 0.1Z_\odot$) versus the fraction of stellar mass that is formed at high-metallicity ($Z > Z_\odot$), for all star formation that occurred below a certain threshold redshift. We compare this to the models from Chruślińska et al. (2021) in Figure 5 in Appendix A. We have chosen our variations such that they span the range of reasonable cosmic metallicity distributions as determined by observation-based and cosmological simulations-based models. For completeness, we furthermore inspect every variation by eye, and make sure none of the variations significantly exceeds the low and high metallicity extremes from Chruślińska et al. (2021).[5]

Lastly, we consider two variations of the overall star-formation history, $\mathrm{SFRD}(z)$, where we keep the metallicity distribution $\mathrm{dP/dZ}(Z, z)$ fixed, but vary all four $\mathrm{SFRD}(z)$ parameters at once (right two columns of Table 1). We use Figure 11 from Chruślińska et al. (2021) to determine approximate upper and lower bounds to the overall star-formation history. We choose Madau & Fragos (2017) as an approximation of the lower limit. For the upper limit, we use the `SB: B18/C17` model variations with a non-evolving low-mass end of the galaxy stellar mass function from Chruślińska et al. (2021)

[3] The phenomenological model from Neijssel et al. (2019) is recovered by adopting $\mu_0 = 0.035$, $\mu_z = -0.23$, $\omega_0 = 0.39$, $\omega_z = 0$, $\alpha = 0$, $a = 0.01$, $b = 2.77$, $c = 2.9$ and $d = 4.7$.

[4] https://github.com/TeamCOMPAS/COMPAS

[5] We compare to the low metallicity extreme model: `214f14SBBiC_FMR270_FOH_z_dM.dat`, and the high metallicity extreme model: `302f14SBBoco_FMR270_FOH_z_dM.dat`.

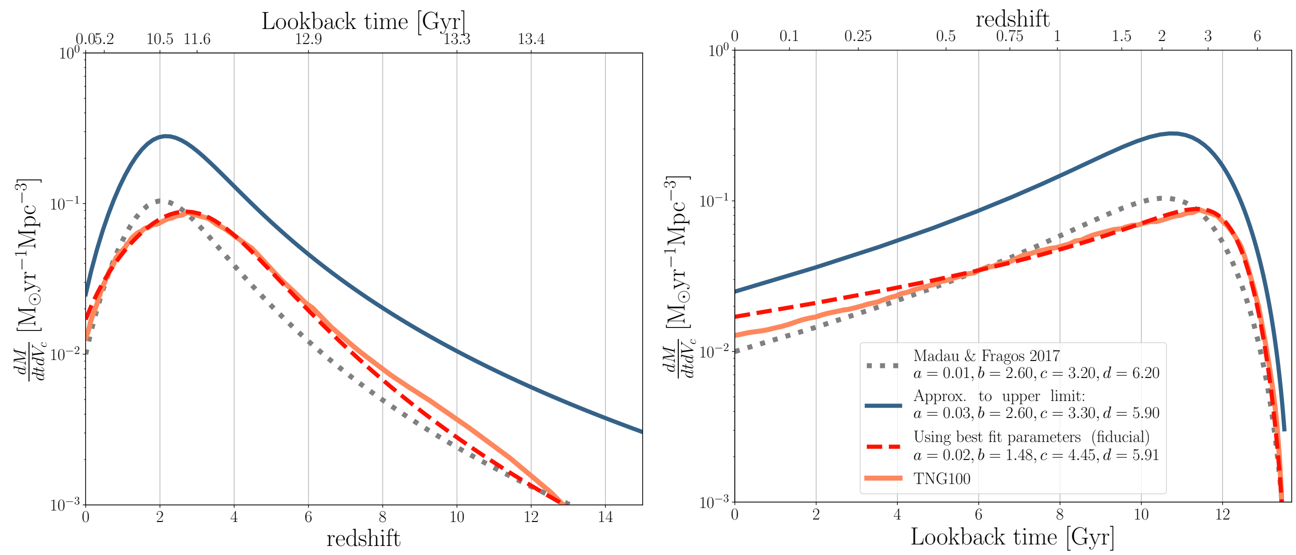

Figure 2. Comparison of different overall star-formation histories with redshift, SFRD(z). The solid orange and dashed red lines respectively show the star formation data from TNG100 and our corresponding fit adopting eq. 12 (fiducial model). The dotted gray and solid blue lines are variations of eq. 12 used to approximate the lower and upper edge of possible star-formation histories. The dotted gray line shows the model from Madau & Fragos (2017), while the solid blue line mimics the behaviour of the powerlaw-fit to the `SB: B18/C17` variations with a non-evolving low-mass end of the galaxy stellar mass function from Chruślińska et al. (2021).

(thick brown line in their Fig. 11). To approximate these models, we fit equation 12 by eye to the broken power law description for the `SB: B18/C17` model variations as presented in appendix B1 from Chruślińska et al. (2021). We show all SFRD(z) variations in Figure 2.

4.2. *The effect of the $\mathcal{S}(Z, z)$ on the primary BH mass distribution*

To isolate the effect of the $\mathcal{S}(Z, z)$ from the effects of different formation channels, we split the data from van Son et al. (2022) between the stable mass transfer channel (e.g., van den Heuvel et al. 2017; Inayoshi et al. 2017; Bavera et al. 2021; Marchant et al. 2021; Gallegos-Garcia et al. 2021; van Son et al. 2022), and the 'classical' common-envelope channel (or CE channel, e.g., Belczynski et al. 2007; Postnov & Yungelson 2014; Belczynski et al. 2016; Vigna-Gómez et al. 2018). These channels are distinguished based on whether the binary system has experienced a common envelope phase (CE channel) or only stable mass transfer (stable channel in short from now on).

In Figures 3 and 4, we show the resulting primary mass distribution of merging BBHs from the stable channel and CE channel respectively. The primary (secondary) component refers to the more (less) massive component of merging BBHs. Each panel varies one aspect of the $\mathcal{S}(Z, z)$.

The first thing we note is that the location of the features in the primary mass distribution are robust against variations in the $\mathcal{S}(Z, z)$. For the CE channel, the global peak of the mass distribution remains at approximately $M_{\rm BH,1} \approx 16 {\rm M}_\odot$ for all variations. Similarly, the stable channel displays two peaks that are visible in all variations: a peak at $M_{\rm BH,1} \approx 9 {\rm M}_\odot$ and a peak at $M_{\rm BH,1} \approx 22 {\rm M}_\odot$. Two more peaks are visible in the stable channel at the high mass end for almost all $\mathcal{S}(Z, z)$ (at $M_{\rm BH,1} \approx 35 {\rm M}_\odot$ and $M_{\rm BH,1} \approx 45 {\rm M}_\odot$), these peaks only fade for variations where the rate of high mass BHs is generally suppressed (dashed lines in top panel of Fig. 3). This is consistent with the results in Broekgaarden et al. (2021b). Although peaks in the probability distribution of chirp masses as shown in their Fig. 4 can disappear when a the $\mathcal{S}(Z, z)$ prohibits the formation of certain (typically higher) mass BHs, the *location* of features remains the same. This result is furthermore consistent with recent findings in Chruślińska (2022). In their Figure 5, they compare two very different models of $\mathcal{S}(Z, z)$ and find that, although the normalisation between the two BBH merger rates is completely different, the location of the peaks remains the same. This implies that the *locations* of features in the mass distribution of BBHs are determined by the formation channel and its underlying stellar and binary physics. The location of features could therefore serve as tell tales of the underlying physics.

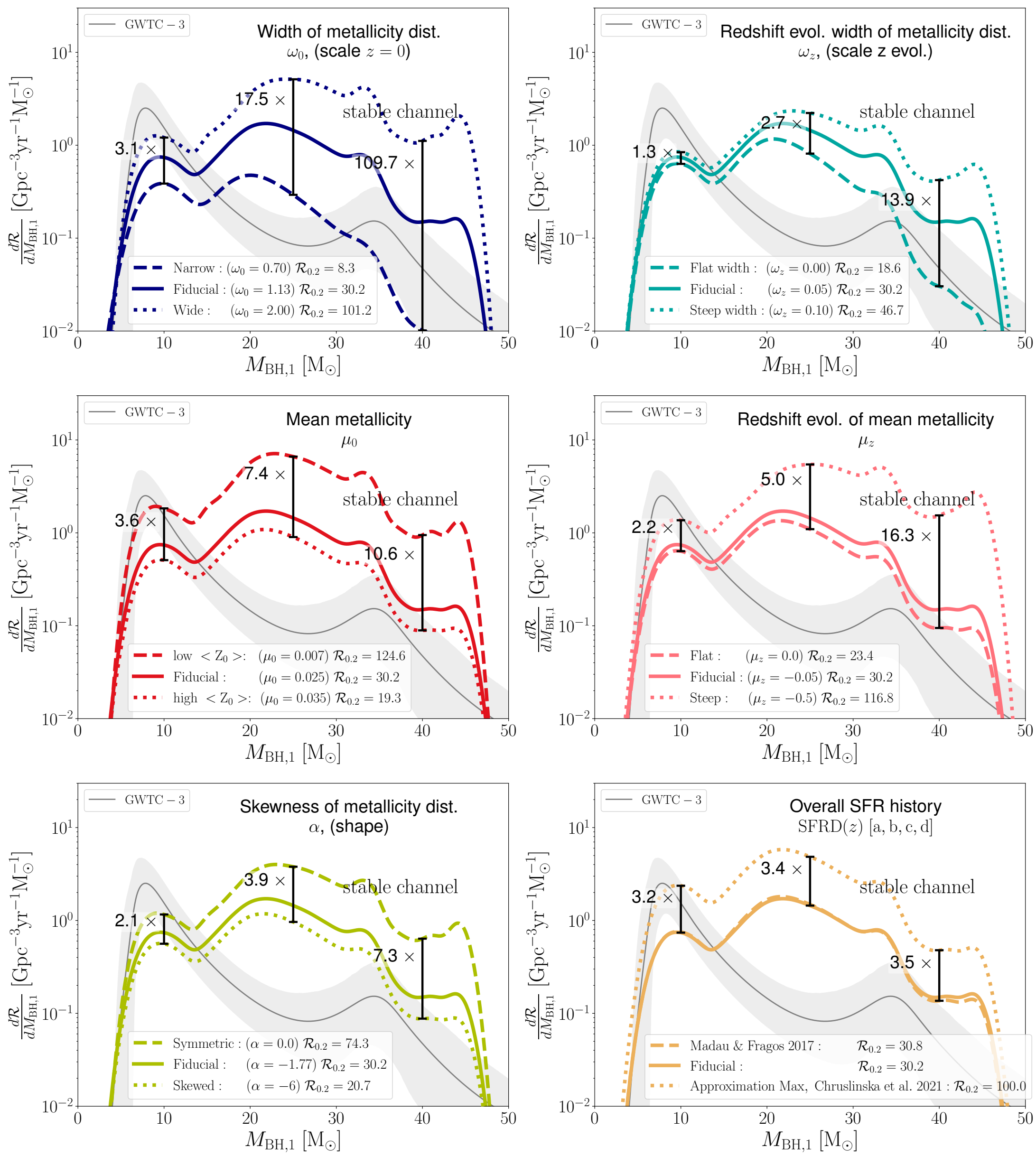

Figure 3. The primary mass distribution of merging BBH systems from the stable mass transfer channel for several variations in $\mathcal{S}(Z, z)$. The first five panels show variations of the cosmic metallicity distribution $\mathrm{dP/dZ}(Z, z)$, eq. 11, (parameters listed in the first three columns of Table 1). The bottom right panel shows variations in the magnitude of the star formation rate with redshift, i.e. SFRD(z). For the latter we vary the four fiducial parameters of SFRD(z) simultaneously (last two columns of Table 1). All panels are shown at a reference redshift of $z = 0.2$, with the corresponding predicted BBH merger rate annotated in the legend. For reference, we show the power-law + peak model from Abbott et al. (2021b) in grey. We annotate the relative change in the rate at three reference masses: $10\mathrm{M}_\odot$, $25\mathrm{M}_\odot$ and $40\mathrm{M}_\odot$.

Second, we see that the low mass end of the primary mass distribution is relatively robust against variations in the $\mathcal{S}(Z, z)$. To quantify this, we annotate the ratio between the maximum and minimum rate at three reference masses; $M_{\rm BH,1} = 10, 25,$ and $40\mathrm{M}_\odot$. At $M_{\rm BH,1} = 10\mathrm{M}_\odot$, we find that the rate changes by at most a factor of about 3.5 for the stable channel, and at most about a factor of 6.5 for the CE channel. On the other hand, the change in rate at $M_{\rm BH,1} = 40\mathrm{M}_\odot$ can be as high as a factor of about 110 and 60 for the stable and CE channel respectively. The low mass end of the mass distribution of merging double compact objects will also provide a particularly powerful cosmological constraint in the era of third generation gravitational wave telescopes (María Ezquiaga & Holz 2022). Our finding that

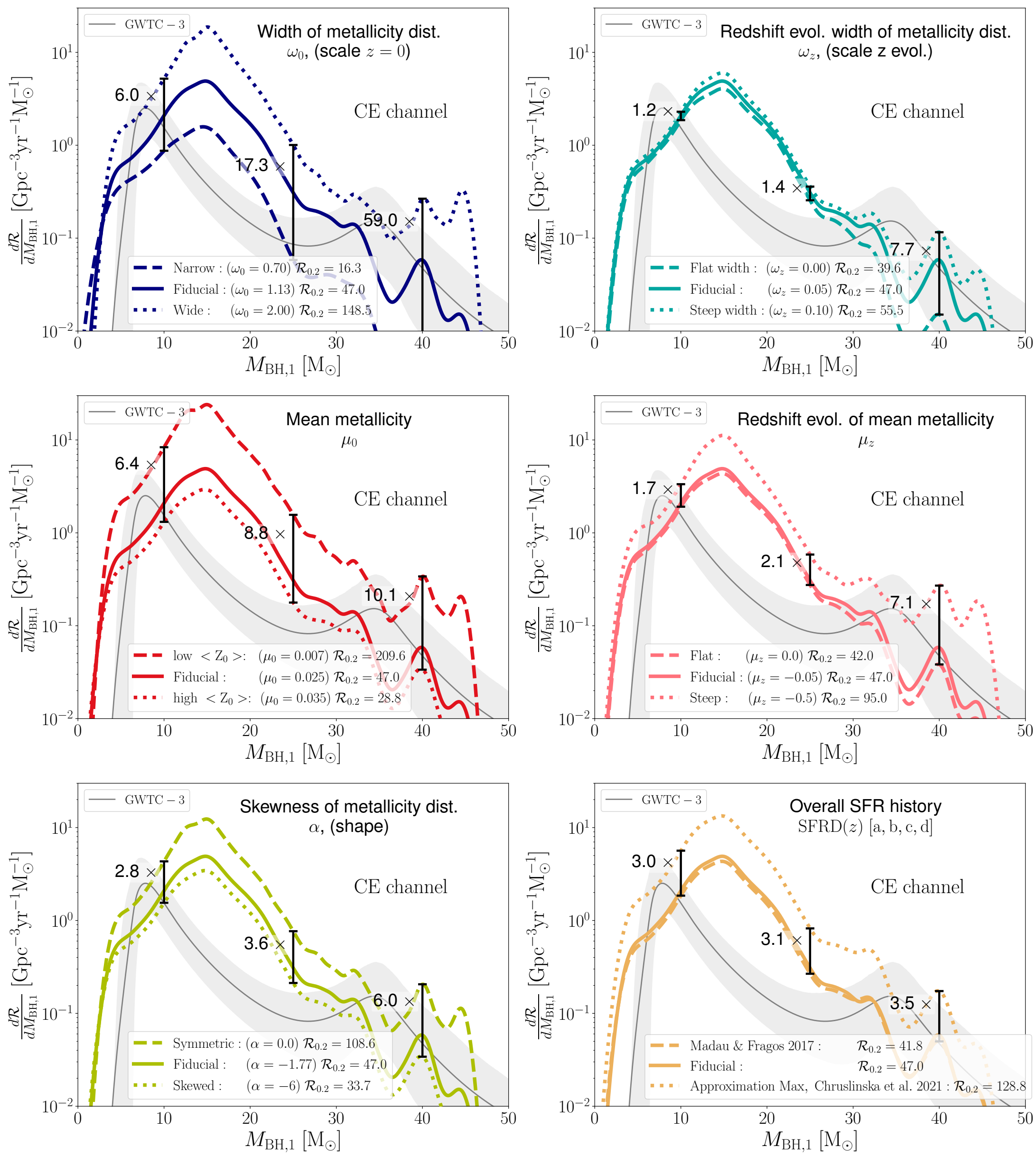

Figure 4. Same as Figure 3, but for the Common envelope channel. These Figures show that the low mass end of the primary mass distribution is least affected by the adopted $\mathcal{S}(Z, z)$. Moreover, the *location* of features in the mass distribution are robust against all explored variations.

the low mass end is more robust against variations in $\mathcal{S}(Z, z)$ supports this claim.

Parameter variations that affect shape of $\mathcal{S}(Z, z)$ at low redshift primarily change the normalisation of the mass distribution. This is the case for variations of the width of the cosmic metallicity distribution at $z = 0$ (ω_0), the mean metallicity of the cosmic metallicity distribution at $z = 0$ (μ_0), and the skewness of the cosmic metallicity distribution (α, left columns of Figures 3 and 4). To emphasise this point, we annotate the total BBH merger rate at redshift 0.2, $\mathcal{R}_{0.2}$, in the legends of Figures 3 and 4 (0.2 if the redshift where the observations are best constrained Abbott et al. 2021b). Variations that *increase* the amount of star formation at low metallicity (i.e. for a low mean metallicity $\mu_0 = 0.007$ and a wide metallicity distribution $\omega_0 = 2.0$) increase the predicted BBH merger rate. This is consistent with other work that finds merging BBHs form more efficiently at low metallicities (e.g. Belczynski et al. 2010; Stevenson et al. 2017; Mapelli et al. 2017; Chruślińska et al. 2019; Broekgaarden et al. 2021b). A more skewed cosmic metallicity distribution pushes the peak of the distribution to higher metallicities and thus forms overall more stars at high metallicity when compared to a symmetric distribution. Hence, the local rate of BBH mergers is lower for the skewed distribution ($\alpha = -6$) with respect to the symmetric variation ($\alpha = 0.0$).

Changing the overall star-formation history (SFRD(z), bottom right panels of Figures 3 and 4) also affects the overall normalisation of the mass distribution, but has a smaller effect than the width and the mean of the cosmic metallicity distribution at $z = 0$ (ω_0 and μ_0). This underlines the importance of the amount of low-metallicity star formation (e.g., Chruślińska 2022), and is furthermore in line with findings from Tang et al. (2020). As discussed in Section 4.1, we use Madau & Fragos (2017) and the solid blue line in Figure 2 as an approximate lower and upper bound to the SFRD(z) respectively. The model from Madau & Fragos (2017) is very similar to our Fiducial model (Figure 2), and the differences between the resulting mass distributions are correspondingly small. Our approximation of the upper limit to the allowed SFRD(z) leads to an overall increase of the BBH merger rate by a factor of about 3.

Parameters that change the evolution of the metallicity distribution dP/dZ(Z, z) with redshift, such as the redshift dependence of the with and mean; ω_z and μ_z (top right and centre right panels of Figures 3 and 4) primarily affect the high mass end of the stable channel. We understand this as an effect of the different delay time distributions for both formation channels. Since both, ω_z and μ_z influence the amount of low metallicity stellar mass formed at high redshifts they will mostly affect systems with longer delay times. The stable channel has been shown to produce more high mass BHs with longer delay times when compared to the CE channel (van Son et al. 2022; Briel et al. 2022). Hence we find these variations affect the slope of the high mass end of the BBH mass distribution for the stable channel, while they have a relatively small impact on the CE channel.

5. DISCUSSION & SUMMARY

We present a flexible analytic expression for the metallicity-dependent star formation rate, $\mathcal{S}(Z, z)$ (equations 1, 11 and 12). An analytical expression allows for controlled experiments of the effect of $\mathcal{S}(Z, z)$ on dependent values, such as the rate and mass distribution of merging BBHs. The model presented in this work adopts a skewed-lognormal for the distribution of metallicities at every redshift (dP/dZ(Z, z)).

The model can capture the general behaviour of cosmological simulations, such as TNG100—Our analytical expression for $\mathcal{S}(Z, z)$ is composed of a cosmic metallicity distribution that is determined by a mean, scale and skewness and their redshift dependence, as well as parameters governing the overall cosmic star formation rate. We fit our analytical expression for $\mathcal{S}(Z, z)$ to the star-forming gas in the TNG100 simulation, and provide the best fit parameters in Table 1. We show that our model captures the shape and general behaviour of the cosmological simulations well (Figure 1).

The model allows for a controlled experiment on the effect of $\mathcal{S}(Z, z)$ on the local distribution of merging BBH—As an example, we apply our model to calculate the local rate and mass distribution of the more massive components from merging BBHs ($M_{\rm BH,1}$) in Figures 3 and 4. We systematically vary all five parameters that shape the cosmic metallicity distribution, and explore two additional variations of the overall star-formation history SFRD(z). Our main findings are as follows:

- The location of features in the distribution of primary BH masses are robust against variations in the $\mathcal{S}(Z, z)$. The location of features in the mass distribution of BHs could thus be used as tell-tale signatures of their formation channel.

- For all variations, the low mass end of the mass distribution is least affected by changes in the $\mathcal{S}(Z, z)$. This suggest that lower end of the BH mass distribution (component masses of $\leq 15 M_{\odot}$) is potentially very powerful for constraining the physics of the formation channels, irrespective of the cosmic star formation rate uncertainties.

- The metallicity distribution of star formation at low redshift, primarily impacts the normalisation of the BBH merger rate. Changing the overall star-formation history, SFRD(z) also affects the rate, but to a lesser degree. This underlines how low-metallicity star formation at low redshifts dominates the overall normalisation of the BBH merger rate.

- Parameters that influence the redshift evolution of the mean and the width of the metallicity distribution, affect the slope of the high mass end of the primary BH mass distribution for the stable channel. This reflects the longer delay times of the stable channel with respect to the CE channel.

The flexibility of the model presented in this work can capture the large uncertainties that remain in the shape and normalisation of the metallicity dependent cosmic star formation history. Our hope is that this expression will provide a useful starting point for making predictions and comparison with observations.

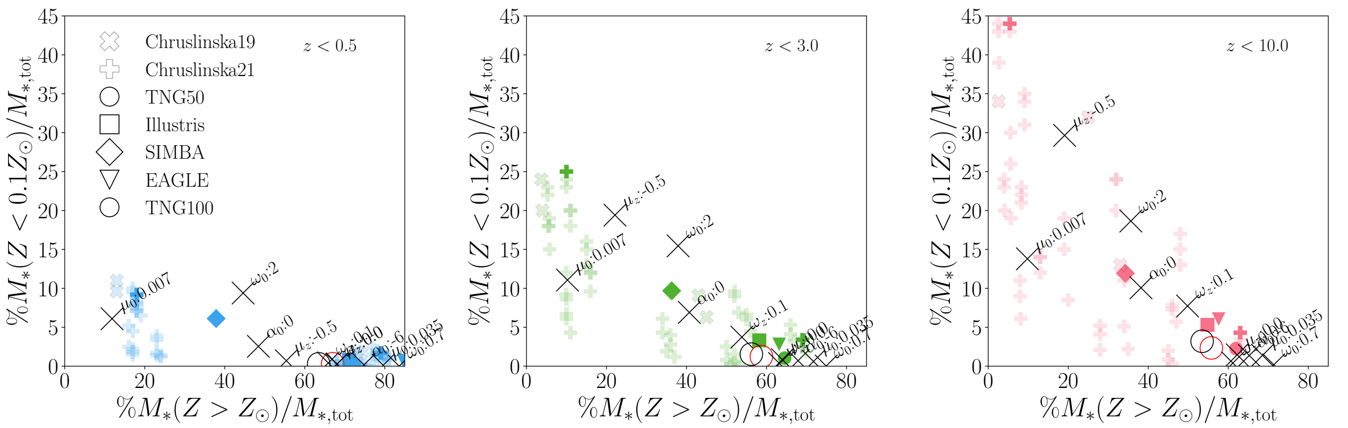

Figure 5. Percentage of stellar mass formed at low metallicity ($Z < 0.1\mathrm{Z}_\odot$) , versus high metallicity ($Z > \mathrm{Z}_\odot$) for all star formation below a certain threshold redshift: $z < 0.5$ (left), $z < 3.0$ (middle) and $z < 10$ (right). Data from observation-based variations are shown with semi-transparent thick crosses, (Chruślińska & Nelemans 2019) and semi-transparent thick plus signs (Chruślińska et al. 2021), the low- and high-metallicity extremes are indicated with opague symbols. For data from cosmological simulations, we follow Pakmor et al. (2022) and show Illustris (Vogelsberger et al. 2014, squares), Simba (Davé et al. 2019, diamonds), EAGLE (Schaye et al. 2015, triangles), TNG50 and TNG100 (Springel et al. 2018, filled and open circles respectively). Black thin crosses display variations of the cosmic metallicity distribution that is part of our fiducial $\mathcal{S}(Z, z)$. The parameter that is varied with respect to the fiducial and its new value are annotated. This shows that our $\mathcal{S}(Z, z)$ variations span the range of reasonable cosmic metallicity distributions as determined by observation-based and cosmological simulations-based models.

The authors acknowledge partial financial support from the National Science Foundation under Grant No. (NSF grant number 2009131 and PHY-1748958)." , the Netherlands Organisation for Scientific Research (NWO) as part of the Vidi research program BinWaves with project number 639.042.728 and the European Union's Horizon 2020 research and innovation program from the European Research Council (ERC, Grant agreement No. 715063).

APPENDIX

A. DETERMINING REASONABLE VARIATIONS OF THE $\mathcal{S}(Z, z)$

To determine reasonable variations of our fiducial model for $\mathcal{S}(Z, z)$, we compute the fraction of low and high metallicity stellar mass formed for redshifts below $z < 0.5$, $z < 3.0$ and $z < 10$. We show the results in Figure 5, which is an adaptation of Fig. 2 in Pakmor et al. (2022), which in turn builds on Fig. 9 from Chruślińska & Nelemans (2019).

REFERENCES

Abbott, B. P., Abbott, R., Abbott, T. D., et al. 2016, ApJL, 818, L22, doi: 10.3847/2041-8205/818/2/L22

Abbott, B. P., et al. 2018, Phys. Rev. https://arxiv.org/abs/1811.12907

Abbott, R., Abbott, T. D., Abraham, S., et al. 2020, arXiv e-prints, arXiv:2010.14527. https://arxiv.org/abs/2010.14527

Abbott, R., Abbott, T. D., Acernese, F., et al. 2021a, arXiv e-prints, arXiv:2111.03606. https://arxiv.org/abs/2111.03606

—. 2021b, arXiv e-prints, arXiv:2111.03634. https://arxiv.org/abs/2111.03634

Bavera, S. S., Fragos, T., Zevin, M., et al. 2021, A&A, 647, A153, doi: 10.1051/0004-6361/202039804

Bavera, S. S., Fragos, T., Zapartas, E., et al. 2022, A&A, 657, L8, doi: 10.1051/0004-6361/202141979

Belczynski, K., Bulik, T., Fryer, C. L., et al. 2010, ApJ, 714, 1217, doi: 10.1088/0004-637X/714/2/1217

Belczynski, K., Holz, D. E., Bulik, T., & O'Shaughnessy, R. 2016, Nature, 534, 512, doi: 10.1038/nature18322

Belczynski, K., Taam, R. E., Kalogera, V., Rasio, F. A., & Bulik, T. 2007, ApJ, 662, 504, doi: 10.1086/513562

Briel, M. M., Eldridge, J. J., Stanway, E. R., Stevance, H. F., & Chrimes, A. A. 2021, arXiv e-prints, arXiv:2111.08124. https://arxiv.org/abs/2111.08124

Briel, M. M., Stevance, H. F., & Eldridge, J. J. 2022, arXiv e-prints, arXiv:2206.13842. https://arxiv.org/abs/2206.13842

Broekgaarden, F. S., Berger, E., Neijssel, C. J., et al. 2021a, arXiv e-prints, arXiv:2103.02608. https://arxiv.org/abs/2103.02608

Broekgaarden, F. S., Berger, E., Stevenson, S., et al. 2021b, arXiv e-prints, arXiv:2112.05763. https://arxiv.org/abs/2112.05763

Chruślińska, M. 2022, arXiv e-prints, arXiv:2206.10622. https://arxiv.org/abs/2206.10622

Chruślińska, M., & Nelemans, G. 2019, MNRAS, 488, 5300, doi: 10.1093/mnras/stz2057

Chruślińska, M., Nelemans, G., & Belczynski, K. 2019, MNRAS, 482, 5012, doi: 10.1093/mnras/sty3087

Chruślińska, M., Nelemans, G., Boco, L., & Lapi, A. 2021, MNRAS, 508, 4994, doi: 10.1093/mnras/stab2690

Crain, R. A., Schaye, J., Bower, R. G., et al. 2015, MNRAS, 450, 1937, doi: 10.1093/mnras/stv725

Cresci, G., Mannucci, F., & Curti, M. 2019, A&A, 627, A42, doi: 10.1051/0004-6361/201834637

Davé, R., Anglés-Alcázar, D., Narayanan, D., et al. 2019, MNRAS, 486, 2827, doi: 10.1093/mnras/stz937

Dominik, M., Belczynski, K., Fryer, C., et al. 2013, ApJ, 779, 72, doi: 10.1088/0004-637X/779/1/72

Dominik, M., Berti, E., O'Shaughnessy, R., et al. 2015, ApJ, 806, 263, doi: 10.1088/0004-637X/806/2/263

Doughty, C., & Finlator, K. 2021, MNRAS, 505, 2207, doi: 10.1093/mnras/stab1448

Dray, L. M., Tout, C. A., Karakas, A. I., & Lattanzio, J. C. 2003, MNRAS, 338, 973, doi: 10.1046/j.1365-8711.2003.06142.x

Farmer, R., Laplace, E., de Mink, S. E., & Justham, S. 2021, ApJ, 923, 214, doi: 10.3847/1538-4357/ac2f44

Fruchter, A. S., Levan, A. J., Strolger, L., et al. 2006, Nature, 441, 463, doi: 10.1038/nature04787

Gallegos-Garcia, M., Berry, C. P. L., Marchant, P., & Kalogera, V. 2021, arXiv e-prints, arXiv:2107.05702. https://arxiv.org/abs/2107.05702

Goswami, S., Silva, L., Bressan, A., et al. 2022, A&A, 663, A1, doi: 10.1051/0004-6361/202142031

Götberg, Y., de Mink, S. E., McQuinn, M., et al. 2020, A&A, 634, A134, doi: 10.1051/0004-6361/201936669

Hemler, Z. S., Torrey, P., Qi, J., et al. 2021, MNRAS, 506, 3024, doi: 10.1093/mnras/stab1803

Hurley, J. R., Pols, O. R., & Tout, C. A. 2000, MNRAS, 315, 543, doi: 10.1046/j.1365-8711.2000.03426.x

Hurley, J. R., Tout, C. A., & Pols, O. R. 2002, MNRAS, 329, 897, doi: 10.1046/j.1365-8711.2002.05038.x

Inayoshi, K., Hirai, R., Kinugawa, T., & Hotokezaka, K. 2017, MNRAS, 468, 5020, doi: 10.1093/mnras/stx757

Kennicutt, Robert C., J. 1989, ApJ, 344, 685, doi: 10.1086/167834

Kewley, L. J., & Ellison, S. L. 2008, ApJ, 681, 1183, doi: 10.1086/587500

Kroupa, P. 2001, MNRAS, 322, 231, doi: 10.1046/j.1365-8711.2001.04022.x

Kummer, F. 2020, UvA Scripties

Langer, N., & Norman, C. A. 2006a, ApJL, 638, L63, doi: 10.1086/500363

—. 2006b, ApJL, 638, L63, doi: 10.1086/500363

Langer, N., Norman, C. A., de Koter, A., et al. 2007, A&A, 475, L19, doi: 10.1051/0004-6361:20078482

Madau, P., & Dickinson, M. 2014, ARA&A, 52, 415, doi: 10.1146/annurev-astro-081811-125615

Madau, P., & Fragos, T. 2017, ApJ, 840, 39, doi: 10.3847/1538-4357/aa6af9

Maiolino, R., & Mannucci, F. 2019, A&A Rv, 27, 3, doi: 10.1007/s00159-018-0112-2

Mapelli, M., Giacobbo, N., Ripamonti, E., & Spera, M. 2017, MNRAS, 472, 2422, doi: 10.1093/mnras/stx2123

Marchant, P., Pappas, K. M. W., Gallegos-Garcia, M., et al. 2021, arXiv e-prints, arXiv:2103.09243. https://arxiv.org/abs/2103.09243

María Ezquiaga, J., & Holz, D. E. 2022, arXiv e-prints, arXiv:2202.08240. https://arxiv.org/abs/2202.08240

Marinacci, F., Vogelsberger, M., Pakmor, R., et al. 2018, MNRAS, 480, 5113, doi: 10.1093/mnras/sty2206

Naiman, J. P., Pillepich, A., Springel, V., et al. 2018, MNRAS, 477, 1206, doi: 10.1093/mnras/sty618

Neijssel, C. J., Vigna-Gómez, A., Stevenson, S., et al. 2019, MNRAS, 490, 3740, doi: 10.1093/mnras/stz2840

Nelson, D., Pillepich, A., Springel, V., et al. 2018, MNRAS, 475, 624, doi: 10.1093/mnras/stx3040

Nocedal, J., & Wright, S. 2006, Numerical optimization, 2nd edn., Springer series in operations research and financial engineering (New York, NY: Springer). http://gso.gbv.de/DB=2.1/CMD?ACT=SRCHA&SRT=YOP&IKT=1016&TRM=ppn+502988711&sourceid=fbw_bibsonomy

O'Hagan, A., & Leonard, T. 1976, Biometrika, 63, 201, doi: 10.1093/biomet/63.1.201

Pakmor, R., Simpson, C. M., van de Voort, F., et al. 2022, MNRAS, 512, 3602, doi: 10.1093/mnras/stac717

Pillepich, A., Nelson, D., Hernquist, L., et al. 2018a, MNRAS, 475, 648, doi: 10.1093/mnras/stx3112

Pillepich, A., Springel, V., Nelson, D., et al. 2018b, MNRAS, 473, 4077, doi: 10.1093/mnras/stx2656

Planck Collaboration, Aghanim, N., Akrami, Y., et al. 2020, A&A, 641, A6, doi: 10.1051/0004-6361/201833910

Pols, O. R., Schröder, K.-P., Hurley, J. R., Tout, C. A., & Eggleton, P. P. 1998, MNRAS, 298, 525, doi: 10.1046/j.1365-8711.1998.01658.x

Postnov, K. A., & Yungelson, L. R. 2014, Living Reviews in Relativity, 17, 3, doi: 10.12942/lrr-2014-3

Riley, J., Agrawal, P., Barrett, J. W., et al. 2022, ApJS, 258, 34, doi: 10.3847/1538-4365/ac416c

Sanders, R. L., Shapley, A. E., Clarke, L., et al. 2022, arXiv e-prints, arXiv:2207.12430. https://arxiv.org/abs/2207.12430

Schaye, J., Crain, R. A., Bower, R. G., et al. 2015, MNRAS, 446, 521, doi: 10.1093/mnras/stu2058

Schmidt, M. 1959, ApJ, 129, 243, doi: 10.1086/146614

Smith, N. 2014, ARA&A, 52, 487, doi: 10.1146/annurev-astro-081913-040025

Springel, V., Pakmor, R., Pillepich, A., et al. 2018, MNRAS, 475, 676, doi: 10.1093/mnras/stx3304

Stevenson, S., Vigna-Gómez, A., Mandel, I., et al. 2017, Nature Communications, 8, 14906, doi: 10.1038/ncomms14906

Tang, P. N., Eldridge, J. J., Stanway, E. R., & Bray, J. C. 2020, MNRAS, 493, L6, doi: 10.1093/mnrasl/slz183

Torrey, P., Vogelsberger, M., Marinacci, F., et al. 2019, MNRAS, 484, 5587, doi: 10.1093/mnras/stz243

van den Heuvel, E. P. J., Portegies Zwart, S. F., & de Mink, S. E. 2017, MNRAS, 471, 4256, doi: 10.1093/mnras/stx1430

van Son, L. A. C., de Mink, S. E., Callister, T., et al. 2022, ApJ, 931, 17, doi: 10.3847/1538-4357/ac64a3

Vigna-Gómez, A., Neijssel, C. J., Stevenson, S., et al. 2018, MNRAS, 481, 4009, doi: 10.1093/mnras/sty2463

Vogelsberger, M., Genel, S., Springel, V., et al. 2014, MNRAS, 444, 1518, doi: 10.1093/mnras/stu1536

Wang, K., Yu, S., & Peng, W. 2019, Journal of Aerosol Science, 134, 95, doi: https://doi.org/10.1016/j.jaerosci.2019.04.013